A Wide Dynamic Range Laser Radar Receiver Based on Input Pulse-Shaping Techniques

Aram Baharmast, *Student Member, IEEE*, Sami Kurtti, and Juha Kostamovaara, *Senior Member, IEEE*

***Abstract*— This paper presents a Time-of-Flight laser radar receiver based on pulse-shaping at the input to the receiver channel, in which the first zero-crossing point of the converted pulse is marked as the timing moment. In this technique, an LC resonator is combined with a nonlinear feedback TIA to achieve high accuracy and high precision within a wide dynamic range. The key advantage is that the receiver does not require any post compensation or gain control techniques so that the total complexity of the TOF radar is reduced considerably. Measurements made in a $0.35\mu m$ standard CMOS process show a bandwidth of $230MHz$ and an input-referred noise of $70nA$ RMS. The receiver chip consumes $155mW$ power from a $3.3V$ supply. The single-shot precision and accuracy of the receiver within a dynamic range of $1:50,000$ are $\sim 15mm (SNR = 12)$ and $\sim \pm 15mm$ respectively. A wider dynamic range can be achieved with a larger accuracy tolerance. The functionality of the proposed receiver channel is also verified over an input pulse variation and temperature range of 0 ^{o}C to 50 ^{o}C.**

***Index Terms*— Time-of-flight, TOF, laser radar receiver, Lidar, timing discrimination.**

I. Introduction

LiDAR (Light Detection and Ranging) is an optical remote sensing technique [1] which was used primarily for military purposes ([2], [3]); but has now found a wide variety of growing applications in industry (e.g. for measuring levels in silos and containers [4], profiling and 2D/3D surface scanning [5], [6]), proximity driving, robotics [7] and airborne laser scanning (ASL) [8], [9].

The basic idea behind pulsed Time of Flight (TOF) LiDAR is to project a short (usually $1-5ns$) pulse of light onto the target and to process the reflected echo(es) to determine the distance (or to profile the target). Since the speed of light is approximately constant (~ 30 cm/ns) under varying environmental conditions, unambiguous resolution at a cm or mm level is readily available even with a single shot measurement at high rates of up to several hundred kHz [10]. This is not possible with continuous wave phase-shifted TOF techniques for example, where the distance is resolved from the phase difference between emitted and detected light signals. Moreover, relative to microwave radars, pulsed TOF techniques provide higher spatial resolution (due to the inherently shorter wavelength of light and ease of control over the optical measurement beam) in ranging applications of up to several hundred meters to non-cooperative targets [10]–[12].

Two important parts of every TOF device are the laser transmitter and the photodetector. The optical pulses generated by the laser should be powerful enough to cover the required dynamic range (DR), whereas in ranging applications the peak power of the laser is limited to below $20-30W$ for practical reasons, e.g. eye safety [3], [13]. High-responsivity ($30-50A/W$) and high gain ($50-100$) avalanche photodiodes (APD) are commercially available and typically used as the photodetector. APDs biased below the breakdown voltage (V_{BR}) region (known as linear mode APDs) are able to detect multiple echoes reflected from several targets and also to measure the intensity of the arriving optical pulses [1], [14]. In this work, an APD is used as the photodetector.

From a general point of view, a TOF receiver (which is the focus of this paper) can be realized based on either sampling-based or event-based approach. In [15] an alternative technique was introduced based on a compromise between these approaches. In the sampling-based approach, an AD converter digitizes the output of the receiver channel. The reflected echoes are then processed in the digital domain. This approach requires a high-speed (e.g. at least $200MS/s$) multi-bit AD converter to achieve reasonable precision, because short pulses and high pulsing rates are typically used [15]. This raises the power consumption issue, especially in multi-dimensional scanning systems, where several multi-channel receivers may be required. In an event-based approach, on the other hand, a time-to-digital converter (TDC) is used to measure the time intervals between the emitted pulse and detected echo, so that no continuous sampling is needed and as a result, the power consumption is considerably reduced. The receiver presented here is based on the event-based approach.

A typical pulsed TOF range finder employing the event-based approach is shown in Fig. 1. The echo pulse received from the APD is amplified and accurately time-discriminated by the receiver channel. The key challenge associated with the receiver channel is to detect the time position of the arriving echo pulse with cm-level (or mm-level) accuracy within the target DR (typically 1:10,000 or more in ranging applications). To accomplish this, the receiver channels introduced in the literature generally have three main functionalities/blocks, as shown in Fig. 1: a) front-end sensing to detect and amplify the current signal coming from the APD.

Manuscript received October 11, 2019; revised December 28, 2019 and February 19, 2020; accepted March 19, 2020. Date of publication April 9, 2020; date of current version July 31, 2020. This work was supported by the Academy of Finland under Contracts 307362 (Centre of Excellence in Laser Scanning Research) and 317144. This article was recommended by Associate Editor Nagendra Krishnapura. *(Corresponding author: Aram Baharmast.)*

The authors are with the Circuits and Systems Research Unit, University of Oulu, 90014 Oulu, Finland (e-mail: aram.baharmast@oulu.fi; sami.kurtti@oulu.fi; juha.kostamovaara@oulu.fi).

Digital Object Identifier 10.1109/TCSI.2020.2983834

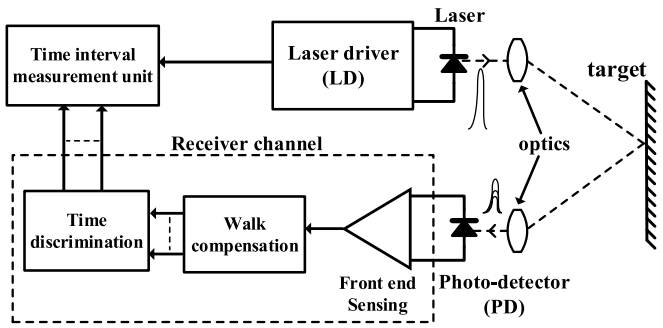

Fig. 1. A typical TOF laser radar system.

b) walk error compensation to minimize the systematic errors associated with TOF ranging systems, and c) timing discrimination, which consists of one or more comparators to convert the timing marks generated by the receiver channel into digital pulses. These functionalities are not necessarily separate blocks, however, depending on the receiver architecture they are embedded in the receiver channel.

The front end should be able to detect the high-speed pulses (e.g. $2-3ns$) coming from the APD accurately, which in turn brings up bandwidth and noise issues. Noise limits not only the sensitivity of the receiver but also single-shot precision, by contributing to the timing jitter. The minimum signal-to-noise ratio (SNR) in ranging applications that keeps the false detection rate at a negligible level is $\sim 8-10$ [4], [16]. The timing jitter, which randomly affects timing detection, is proportional to the rise time of the arriving pulse [17] so that shorter pulses give better precision but it calls for a receiver with a wider bandwidth [18]. Most of the proposed circuits for the front end are based on trans-impedance amplifiers (TIA): i.e. shunt feedback-based [1], [19]–[26] and current mode-based [4], [27]–[30] TIAs. A combination of both approaches has been employed in [31]. Shunt feedback-based TIAs have gained more attention, however, due to their unique properties of low noise, low input impedance, and relatively wide bandwidth [32]. A shunt feedback Capacitor-TIA was adopted in [33] for instance, in order to reach a very low noise level of $1.6pA/\sqrt{Hz}$.

Another source of inaccuracy in pulsed TOF range finders known as walk error, which is the deviation in the timing point with pulse amplitude. Reflected echo pulses in distance ranging applications can vary in a range of 1:10,000 or even more depending on the distance, the reflectivity of the target, environmental conditions and the angle of the target relative to the TOF device. If a comparator with a constant threshold voltage is used to mark the timing moment (known as leading-edge detection method), a considerable amount of walk error will be generated. The walk error has two main sources: variations in pulse rise time with the amplitude of the pulse (known as geometric walk error, which remains even with an ideal comparator) and nonlinear variation in the electronic delay of the receiver for different pulse amplitudes [34]. To mitigate this issue a walk compensation scheme is usually adopted. In leading-edge based receivers various pulse characteristics such as amplitude ([12]), pulse width ([22]), slew rate and/or rise time ([20], [23]) are discriminated and used to compensate for the walk error. These techniques provide a wide DR ($>$1:10,000) with a low walk error (e.g. $<$ 50ps), but they need relatively complicated calibration methods in collaboration with a multi-channel TDC. A recent implementation example of this technique was presented in [20], [21]. Another approach is to employ electronic gain control, either within the input stage or as a separate block [1], [25], [27], [30], [31]. This technique suffers from a limited DR (typically 1: ~500-1500), however, due to the non-constant delay in the gain control electronics. Optical gain control is another solution but it is usually slow and bulky.

A further technique introduced to compensate for walk error is to convert the unipolar current pulse detected by the APD to a bipolar signal at the input to the receiver channel and then pick out the zero-crossing point of the converted signal as the timing mark. The idea behind this approach is that the receiver channel should return to its linear region near the zero-crossing point so that clipping of the signal at high input levels will have little effect on the timing moment and a wide DR can be achieved. This can be accomplished if the receiver channel is fast enough to recover from clipping [35]. This technique has been implemented at the circuit level using either a high-pass RC differentiator or an RLC-based resonator [28], [35]. The high-pass RC differentiator alternative cannot be implemented next to the input node because the parasitic capacitance of the photodetector will destroy the high-pass filtering. Consequently, the RC filter is placed after the front end, in which case its limited DR restricts the DR of the whole receiver channel [28]. The RLC-based pulse shaping proposed in [35], on the other hand, converts the APD current pulse to a bipolar voltage signal at the input node and then amplifies the converted voltage through the receiver channel. This nevertheless places practical limitations on the DR at both the low and the high end. At the low end, the relatively small damping resistor used at the input produces a large amount of noise, which in turn limits the sensitivity of the receiver, while at the high end the early current-to-voltage conversion at the input node limits the maximum permitted input current.

This paper presents a CMOS laser radar receiver based on a new implementation of the pulse-shaping approach in which an LC resonator is combined with a nonlinear shunt feedback TIA. The proposed receiver achieves a DR of $\sim 1:50,000$ while its accuracy is better than $\pm 100ps(\pm 15mm)$ and the single-shot precision is $\sim 100ps$ $(15mm)$ for an SNR of 12. As the only timing parameter discriminated here is the zero-crossing point of the bipolar signal, the receiver does not require any specific calibration or compensation technique as is typically needed in state-of-the-art TOF receivers. This is a key advantage that considerably reduces the total complexity of the proposed TOF system. The paper is organized as follows. The operation principle and design issues are discussed in section II, section III is devoted to the circuit-level realization of the whole receiver channel, measurement results are shown in section IV and

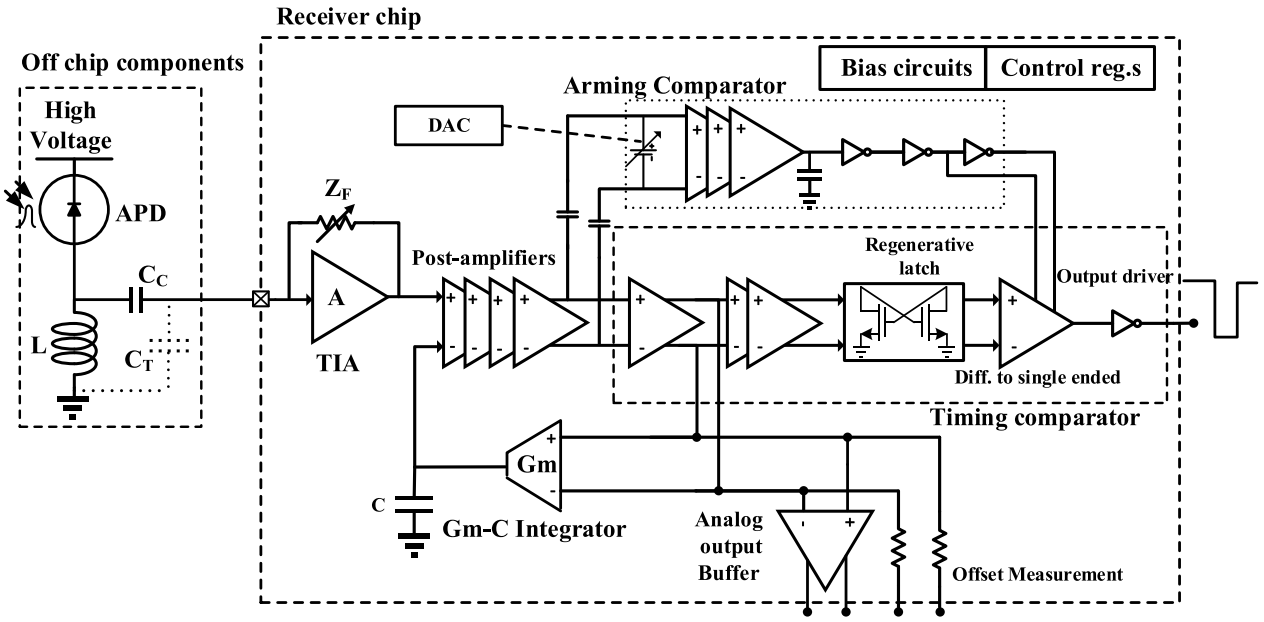

Fig. 2. Block diagram of the proposed receiver channel.

a discussion and the conclusions to be drawn are given in section V.

II. Receiver Channel Architecture

A block diagram of the proposed TOF receiver channel is shown in Fig. 2. The APD used here ($TO52S1AD230$) has an active area of $0.04mm^2$ ($230\mu m$ diameter) and provides a high internal gain (e.g. 100) when biased below its breakdown voltage ($\sim 140V$). The "unipolar" current pulses of $\sim 2-3$ ns Full Width at Half Maximum (FWHM) detected in the APD are converted to a "bipolar" voltage by passing through an off-chip LC resonator and front-end nonlinear feedback TIA. The bipolar signal is amplified through the receiver channel and its "first zero-crossing point" is detected in order to trigger a "stop" in the TDC. A Gm-C integrator is embedded in the receiver to cancel out the offset through the channel. An analog buffer is also used to measure the gain, noise and bandwidth of the channel.

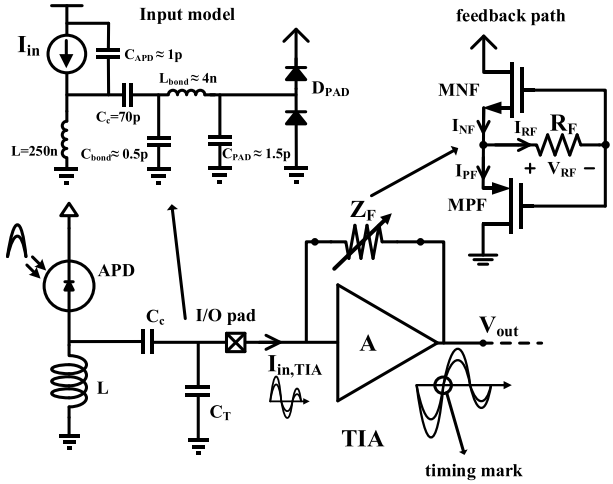

Fig. 3. A block diagram of the nonlinear feedback TIA front end. The size of the parasitic elements are approximate values used to model the input node.

A. Design Principle of the Front End

A simplified block diagram of the front end is shown in Fig. 3. The input circuitry includes an off-chip inductor which is connected to the anode of the APD diode. As can be seen, no bias resistors are used in the front end. The inductor forms an LC resonator with the parasitic capacitances of the APD, bonding wires, PAD and input transistor of the TIA. The total amount of this capacitance (C_T) affects the performance of the whole system in terms of bandwidth, noise and walk error. Here a commercial high-frequency RF inductor ($0603HP-R25$) is used. Its specifications include a quality factor of 45 in the 250 MHz frequency range (employed frequency range), and a self-resonance frequency (SRF) of 1 GHz. These characteristics indicate low enough parasitics (series resistance and stray capacitance) for the inductor in the intended application.

The current pulse of the APD excites the LC resonator to produce an oscillating signal current which flows into the TIA feedback path. Thus the feedback resistance of the TIA acts both as a damping element for the RLC resonator and as a pass to convert the resulting current into a voltage at the output of the TIA. Since the first zero-crossing point marks the timing point, the RLC circuit should provide a fast, underdamped response that damps the resulting oscillation after one or two cycles. The resistance seen at the input of the TIA (i.e.$R_{in,TIA}$) can be calculated as

$$R_{in,TIA} = \frac{Z_F}{A_0 + 1}, \tag{1}$$

where Z_F is the resistance of the feedback path and A_0 is the DC gain of the core amplifier (A). The feedback path consists of a passive resistor (R_F) and two auxiliary transistors as shown in Fig. 3. For the linear region of the TIA (small input currents), Z_F is equal to R_F. The function of these auxiliary transistors will be discussed later in section II-2.

Based on (1), a higher feedback resistance can be used, while proper damping can be set via the gain of the core amplifier, although practical circumstances limit the choice of the gain and feedback resistor and of the off-chip inductor (L). The first factor involved here is the required bandwidth, which should be high enough to preserve short pulses of $2-3ns$. Since a large capacitance is seen at the input node, the dominant pole of the receiver is located at this node. Other limitations arise from the noise and walk error. The various characteristics of the front end will be discussed in the following subsections.

1) Linear Region Analysis: As long as the input current to the TIA is small enough to ensure that the voltage drop over the feedback resistor (R_F) is below the threshold voltage of the two auxiliary transistors (M_{NF} and M_{PF}), the core amplifier (A) will remain in its linear region and can be modeled as a single-pole inverting voltage amplifier. Assuming such a model for the core amplifier, the total trans-impedance gain can be found as

$$Z_T(s) = \frac{V_{out}}{I_{in}} = -\frac{N(s)}{D(s)}, \tag{2}$$

and

$$N(s) = \frac{A_0\omega_2}{C_T}s, \tag{3}$$

$$D(s) = s^3 + \left(\omega_2 + \frac{1}{R_F C_T}\right)s^2 + \left(\frac{(A_0+1)\omega_2}{R_F C_T} + \frac{1}{LC_T}\right)s + \frac{\omega_2}{LC_T}, \tag{4}$$

where ω_2 is the high-frequency pole of the core amplifier and C_T is the total input capacitance at the input node. Note that in the presence of ω_2, $D(s)$ is a third-order function of s. ω_2 should be chosen to be high enough to ensure a flat response in the frequency ranges in which the pulse shaping occurs. On the other hand, a very high bandwidth core amplifier would result in excessive noise, which is not desirable. In practice, to ensure a maximally flat frequency response in the TIA (not the whole pulse shaper), we should have ([36], [37]):

$$\omega_2 \geq 2\omega_{\mathrm{u}} \approx \frac{A_0}{R_{\mathrm{F}}C_T} + \sqrt{\frac{4}{LC_T} + \left(\frac{A_0}{R_{\mathrm{F}}C_T}\right)^2}, \tag{5}$$

where ω_{u} is the unity gain frequency of the front end. In this case, the $-3dB$ bandwidth of the TIA channel will be

$$\omega_{-3\mathrm{dB}} \cong \frac{A_0+1}{2R_{\mathrm{F}}C_T} + \sqrt{\frac{1}{LC_T} + \left(\frac{A_0+1}{2R_{\mathrm{F}}C_T}\right)^2}, \tag{6}$$

which is equivalent to the upper cut-off frequency of a parallel RLC circuit when its resistance is equal to (1). This equation reveals the roles of the core amplifier gain and the input node capacitance in the bandwidth of the receiver channel. As seen in (6), a large inductor will also limit the bandwidth.

It is well known that in band-limited communication systems for a given rise time (t_r) of the arriving pulse the bandwidth of the receiver that preserves the fast edge of that pulse should be [38]

$$BW = \sim \frac{0.35}{t_r}, \tag{7}$$

Increasing the bandwidth by more than this value will increase the in-band noise without any significant improvement in the preservation of the fast edge. Even though the proposed receiver is based on front-end pulse shaping, which is inherently a bandpass system, our simulations and measurements show that the value of the bandwidth given by (6) is comparable to (7) and is a good measure for evaluating the required bandwidth of the channel.

Without the two auxiliary transistors (M_{NF} and M_{PF} in Fig. 3), the proposed front end works well only within the linear region of the core amplifier. The transient simulation shows that in this region the deviation of the zero-crossing point for different input pulse amplitudes (which represents the walk error) is negligible. Once the input current exceeds a certain threshold, however, and drives the core amplifier to the nonlinear region, the walk error will start to increase dramatically. Furthermore, the output signal will tend to oscillate. This is because the input damping given by (1) is no longer valid in this region and the front-end does not work according to the expected linear circumstances [39].

2) Nonlinear Region Analysis: As the input current of the TIA increases and the voltage drop over the feedback resistor comes to exceed the threshold voltage of the auxiliary transistors,

$$|V_{RF}| = \left|V_{GS-NF,PF}\right| \geq \left|V_{TH-NF,PF}\right|, \tag{8}$$

The two transistors eventually turn on and sink the extra current in the ground (M_{PF}) or source it from the power supply (M_{NF}). Large signal analysis using the square characteristic of the MOS transistor in this region reveals that the current flowing to the feedback resistor (which produces the output voltage of the TIA) is no longer equal to the input current $I_{in,TIA}$ but instead is proportional to the square root of it: ($I_{RF} \propto \sqrt{I}_{in,TIA}$). This is shown in the Appendix and can be seen in Fig. 4, in which the current flowing into the feedback resistor is plotted as a function of the input current for a conventional TIA and the proposed nonlinear feedback TIA. It is clear from this figure that the two transistors prove useful in preventing the TIA from being deeply saturated by providing a detour to the excessive input current. The resistance of the feedback path in this region is equal to

$$Z_F = R_F \parallel \frac{1}{G_{mF}}, \tag{9}$$

and

$$\begin{cases} G_{mF} = G_{m,NF} \\ \quad = K_N\left(V_{GS,NF} - V_{TH,N}\right) & -V_{RF} \geq V_{TH,NF} \\ G_{mF} = G_{m,PF} \\ \quad = K_P\left(V_{SG,PF} - |V_{TH,P}|\right) & V_{RF} \geq |V_{TH,PF}| \end{cases}, \tag{10}$$

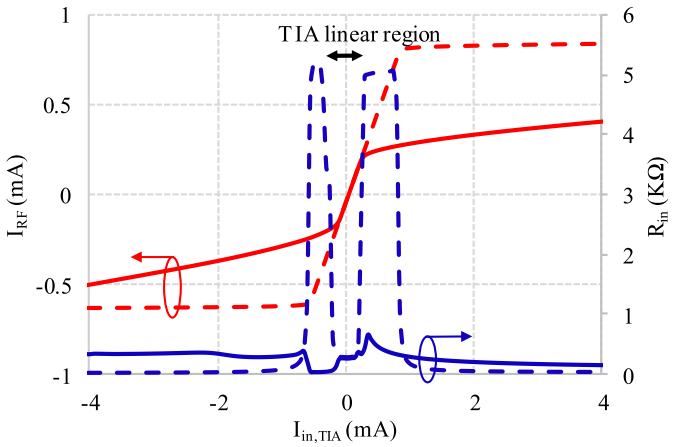

Fig. 4. The current flowing through R_F (red) and TIA input resistance $R_{in,TIA}$(blue) versus the input current of the TIA. The solid lines represent nonlinear feedback TIA and the dashed lines represent conventional linear feedback TIA.

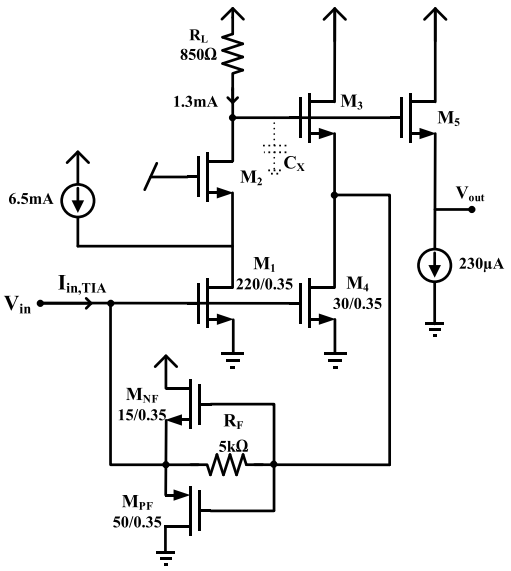

Fig. 5. Circuit-level realization of the TIA.

where $G_{m,NF}$ and $G_{m,PF}$ are the transconductances of M_{NF} and M_{PF}, respectively, and K_N and K_P are the transconductance parameters of those transistors, respectively. The aspect ratios of these transistors (50/0.35 and 15/0.35 for M_{PF} and M_{NF}) are such that they demonstrate a much smaller resistance than the R_F for the very large input signals in the region of which the gain in the core amplifier is heavily suppressed, and consequently the input resistance is determined by these two transistors ($R_{in,TIA} = Z_F \approx 1/G_{mF}$). This is shown in Fig. 4, too, where the input resistance of the TIA is plotted as a function of the input current with and without these two auxiliary transistors. According to this figure, the variation in the input resistance is much lower in the proposed nonlinear feedback TIA than in the conventional TIA and the damping is preserved effectively within a wide range of input currents. These two transistors continue to shunt the extra currents until the protection diodes embedded in the input PAD (D_{PAD} in Fig. 3) clamp the TIA input voltage. Simulations indicate that, for the design parameters of 20, $5k\Omega$ and $250nH$ for A_0, R_F and L, respectively, this happens with APD input currents as large as $\sim 30mA$. This technique effectively controls the deviation in the zero-crossing point within a wide range of the input currents.

III. Circuit Level Realization

A. The TIA

The circuit-level realization of the TIA is shown in Fig. 5. The core amplifier consists of a boosted cascode stage with the resistor load and a common source stage, and these are combined together in a feed-forward manner. Almost all the gain takes place in the cascode stage, however, as the gain of the common source stage is set to ~ 1. When a large input current drives the core amplifier to saturation, this stage will recover from saturation prior to the cascode stage. Simulations show that this technique improves the walk error in the presence of a large I/O PAD capacitance at the input node [40].

In accordance with this configuration, the high-frequency pole of the core amplifier (ω_2) is located at the drain of M_2 (high impedance node of the core amplifier) and is equal to

$$\omega_2 = \frac{1}{R_L C_X}, \tag{11}$$

where C_X is the stray capacitance of the metal layers and the parasitic capacitance of the transistors M_3, M_5 and M_2.

The main noise contributors at the input to the receiver channel are the noise due to the APD itself (i.e. that generated by the signal current and the dark current of the APD), shot noise from the background illumination and the electronic noise of the receiver channel, the last-mentioned usually being dominant, especially at low signal levels. The dominant electronic noise sources in the whole receiver channel are the input transistor of the TIA (M_1) and the feedback resistor (R_F). The auxiliary transistors (M_{NF} and M_{PF}) are turned off for small signal levels, and therefore, their impact on the noise behavior of the front end is negligible. Since we have an LC circuit at the input, the voltage noise at the output of the TIA can be calculated as:

$$\frac{\overline{V_{n,out}^2}}{4kT} \approx \frac{1}{R_F}\left|\frac{N(s)}{D(s)}\right|^2 + \left|g_{m1}R_L\omega_2\frac{s^2 + \frac{1}{R_F C_T}s + \frac{1}{LC_T}}{D(s)}\right|^2 \frac{\gamma}{g_{m1}}, \tag{12}$$

where g_{m1} is the transconductance of M_1 and $g_{m1}R_L$ is equal to the gain of the core amplifier (A_0). γ is the noise parameter, which in the technology used here can be estimated to be 2/3. k and T are the Boltzmann constant and the temperature in degrees Kelvin, respectively. The first term represents the thermal noise of the feedback resistor and has a bandpass nature around the resonance frequency that is similar to the transimpedance gain (Z(s)). This is because the current noise of the feedback resistor goes through the same path as the input current. The bandpass nature of the feedback resistor noise improves the total SNR, however, because the important part of the converted signal is located within the bandwidth of the bandpass filter while the white noise spectrum of the resistor is filtered out at both high and low frequencies.

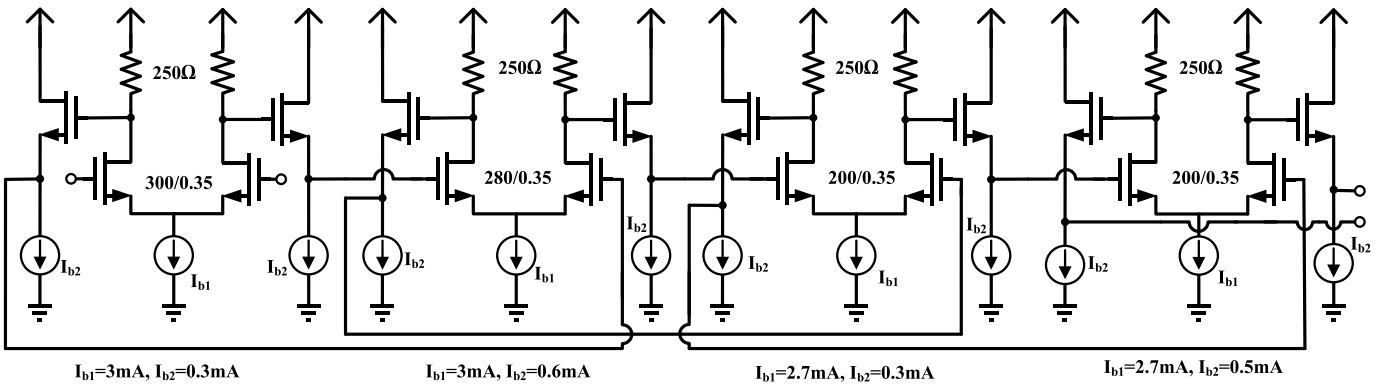

Fig. 6. Structure of the post-amplifiers.

The second term in (12) represents the noise voltage due to the channel thermal noise of the input transistor (M_1). The noise generated by other components of the core amplifier is neglected. This term has a band-stop nature, due to the fact that the inductor (L) at low frequencies and the capacitor (C_T) at high frequencies will provide a low impedance pass to the ground and allow the noise of the input transistor to be amplified by A_0 [36], [41].

For precise detection of the incoming pulse, it is important to minimize the total RMS noise at the input to the timing comparator [16] by limiting the high-frequency noise. As mentioned above, the LC resonator rolls off the high-frequency noise of the R_F resistor, but it does not attenuate that of the core amplifier. For this reason ω_2 should be chosen to be low enough with respect to (5), since it rolls off the high-frequency noise of both electronic noise contributors. Another consideration, however, is the walk error, which requires that the core amplifier should be fast enough to recover from saturation in the case of large input signals. There is, therefore, a trade-off between noise performance and the walk error. In this design ω_2 was chosen to be $\sim 2\pi \cdot 800MHz$.

Referring the output noise (12) to the input of the receiver channel according to (Z(s)) results in:

$$\overline{I_{n,in}^2} = \frac{\overline{V_{n,out}^2}}{|Z_T(s)|^2} \approx \frac{4kT}{R_F} + \left|\frac{1}{Ls} + \frac{1}{R_F} + C_T s\right|^2 \frac{4kT\gamma}{g_{m1}}, \quad (13)$$

The first term can be minimized by increasing the feedback resistance, although at the cost of a lower bandwidth (6). As mentioned previously, R_F was set to $5k\Omega$ in this design and the bandwidth was adjusted by reference to the core amplifier gain.

According to the second term in (13), the dominant components affecting the noise contribution of the core amplifier at low, middle and high frequencies are L, R_F and C_T, respectively. To minimize the noise, L, R_F and g_{m1} should be maximized while C_T should be minimized taking the target bandwidth (equation 6), pulse shape (width and rise time) and the walk error into consideration. Although increasing L limits the signal bandwidth, g_{m1} can be maximized by increasing either the aspect ratio $(W/L)_{M1}$ or the bias current of M_1. Here an extra bias current of $6.5mA$ was added to the cascode stage to boost g_{m1}. On the other hand, increasing the $(W/L)_{M1}$ results in an increase in C_T. Since at high frequencies the noise increases as a function of frequency, it is important to choose the optimum size for the input transistor in order to minimize the noise peaking ([37], [42]). As mentioned in section II-A, the target pulse shape defines the required signal bandwidth. The noise should be minimized while reaching the target bandwidth, underdamped response of the input RLC network and minimum possible walk error. In this design, the inductance L was set to $250nH$ in the presence of a measured total input capacitance (C_T) of $\sim 4pF$.

B. Post-Amplifiers

A chain of post-amplifiers is used to further amplify the output voltage of the TIA in order to provide enough voltage swing at the input to the timing comparator. These amplifiers should be fast enough to recover from saturation at high input levels, even though their bandwidth should be limited due to noise considerations, as was mentioned above. A multistage solution provides multipoles and consequently filters the high-frequency noise by a higher rate. the optimum number of stages and type of employed structure (e.g. first order amplifier with one real pole or a second order one with two complex poles) depends on the required total gain and target bandwidth [43]. Since the post-amplifiers are mostly working in the clipping mode (and not in their linear region, especially later stages), for a given total gain (A_{tot}) the optimum number of stages that gives an optimized gain-bandwidth product (GWB) is ($n = ln(A_{tot})$) where the gain per stage should be $\sim$ e(≈ 2.718) [44]. Here, the post-amplifiers are implemented using four-stage low-gain ($\sim 8 - 10dB$ each) high-bandwidth ($\sim 1GHz$ each) differential amplifiers. Shown in Fig. 6, each stage consists of a resistor load differential amplifier followed by one stage of source follower. The use of source followers relaxes the loading effect of the following stage on the high-impedance nodes and simplifies the design of each individual stage. Furthermore, this structure proves useful in passing the bipolar signal without affecting the zero-crossing point.

C. The Timing Discriminator

The timing discriminator consists of two comparators: an arming comparator and a timing comparator, as shown

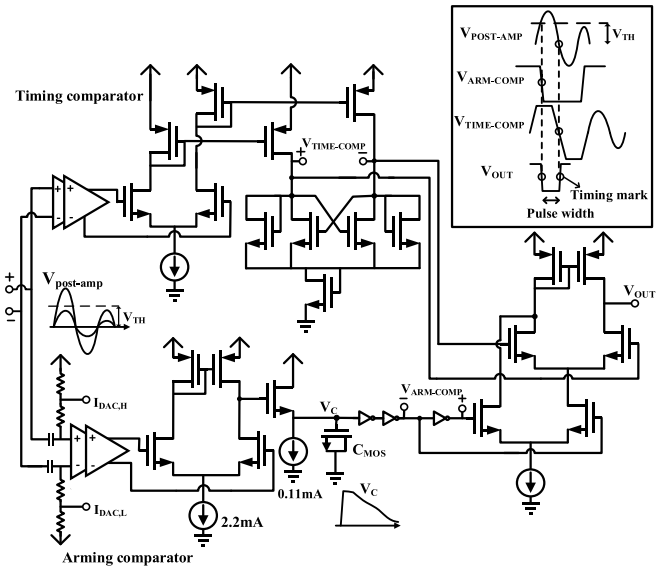

Fig. 7. The structure of the timing discriminator and corresponding timing diagram.

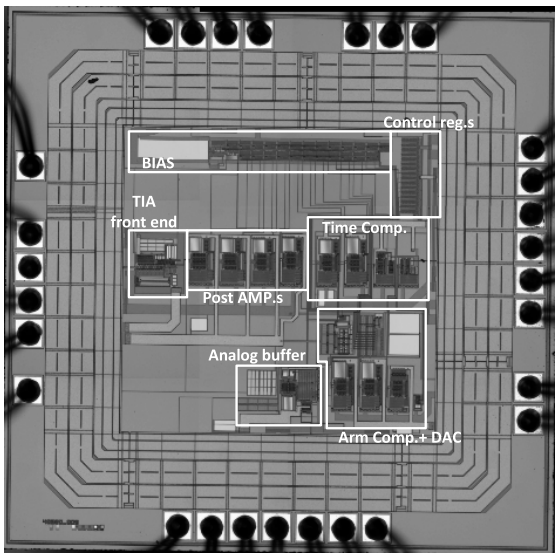

Fig. 8. Die microphotograph of the receiver channel.

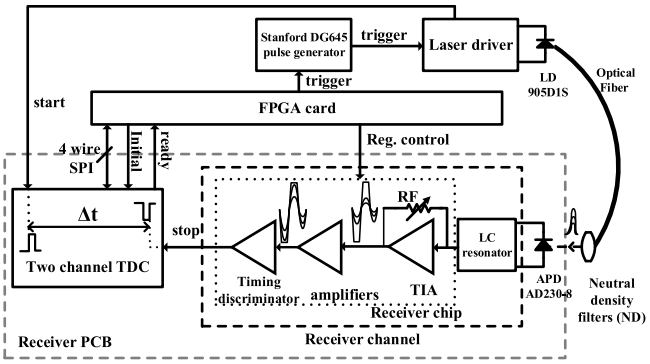

Fig. 9. Measurement setup.

in Fig. 7. The arming comparator enables the timing comparator for valid signals, i.e. those that exceed a predefined threshold voltage, which is controlled digitally through a DAC (Digital to Analog Converter). It is usually set according to the noise level at the input to the arming comparator.

Both the arming comparator and the timing comparator employ primarily two differential post-amplification stages similar to those of the post-amplifier. Since the input overdrive voltage of the arming comparator is less than that of the timing comparator, the output signal of the former is delayed for small input amplitudes [45]. This delay should be small enough that the arm signal does not interrupt the timing moment, which lies at the next zero-crossing point of the input signal. The delay decreases, however, as the amplitude of the input signal increases. The amplified signal of the arming comparator is fed to a MOS capacitor (C_{MOS}) through another differential to single-ended stage, the tail current of which ($2.2mA$) is large enough to charge this capacitor rapidly while the current source tied to the capacitor ($110\mu A$) discharges it at a very slow pace. This technique produces a wide enable pulse at the output of the arming comparator that remains active during the zero crossings of the timing signal. The amplified signal in the timing comparator is fed to a regenerative latch to produce a full swing signal that generates the final digital pulse. A timing diagram showing the synchronization between the various parts of the timing discriminator is also shown in Fig. 7. As can be seen, the width of the output pulse is affected by the arming comparator, but the final timing mark is defined by the zero-crossing point of the signal.

IV. Measurement Results

The proposed TOF receiver was fabricated in standard 0.35μm CMOS 4 metal technology. A photograph of the fabricated die including pads is shown in Fig. 8. Its dimensions are $1.7mm \times 1.7mm$. The receiver chip was enclosed in a QFN24 package. The receiver channel consumes $47mA$ of current from a $3.3V$ supply. When the analog buffer is enabled the current consumption rises by a further $8mA$.

A block diagram of the measurement environment used as a TOF laser radar system to evaluate the performance of the receiver channel is shown in Fig. 9. The whole process, which includes initializing the TDC, sending a trigger pulse to the laser driver through the pulse (delay) generator, reading the measurements from the TDC and programming the registers of the receiver channel, is governed by an FPGA card. The optical pulses of the laser are fed to the APD through an optical fiber and a set of neutral density filters (THORLABS NEK01). The variation in the input pulse amplitude is emulated by means of these optical filters.

The time interval measurement unit employed here was a two-channel TDC with an LSB of $\sim 10ps$ [46], although in our experiments just one channel was used. Since no post-compensation or calibration is needed, this receiver channel can be integrated with a simplified TDC channel in a single die.

A. Analog Measurements

The analog properties of the channel were measured through the analog buffer. This is a differential source-degenerated

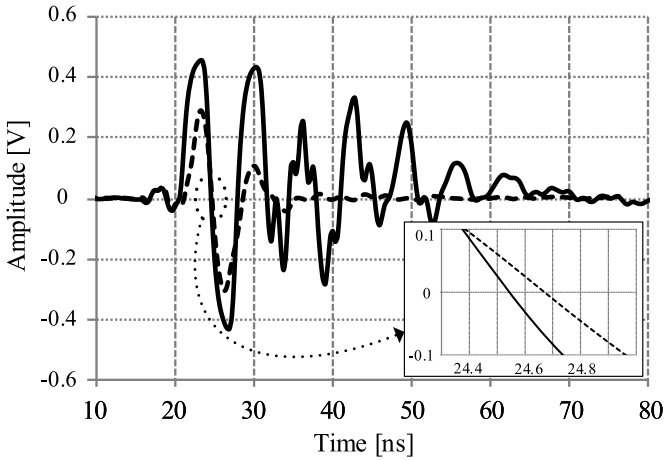

Fig. 10. Sample analog output for a linear (dashed line) and strongly saturated channel (solid line).

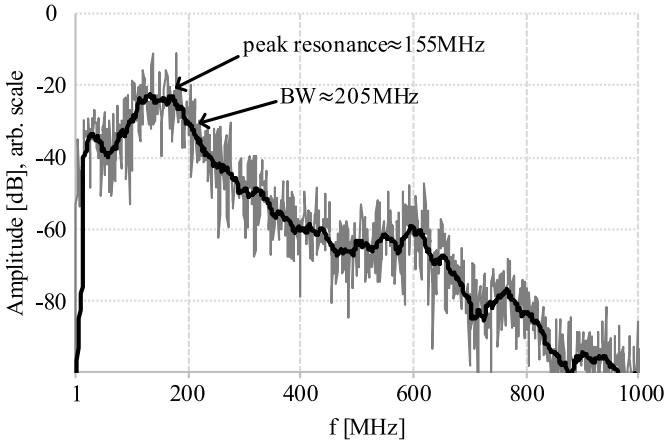

Fig. 11. Measured frequency response of the receiver channel.

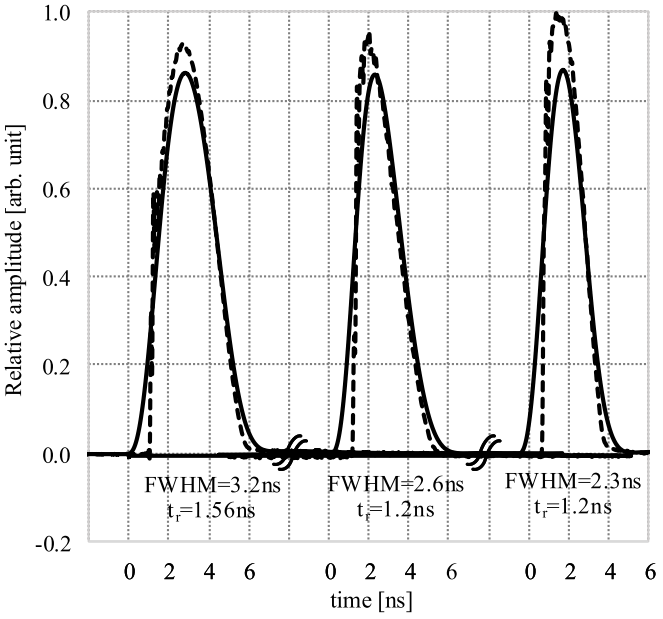

Fig. 12. Three different pulse shapes used in measurements. The dashed lines show unfiltered version of the pulses measured with a high-speed optical detector (oscilloscope bandwidth = 8 GHz).

stage followed by two source follower stages that have a gain of ~ 1 with a bandwidth of $\sim 1GHz$ in the presence of a large PCB and output PAD parasitic capacitance. All the analog measurements were performed using a 1 GHz KEYSIGHT MSOX3104T oscilloscope and a 3.5 GHz Agilent 1131A active probe system.

Typical output signals measured from the analog output buffer are shown in Fig. 10 for small and very large input amplitudes. As can be seen in both cases, pulse-shaping clearly takes place. The deviation of the zero-crossing points, which corresponds to the walk error is also shown. It should be noted, however, that this measurement cannot be referred to evaluate the walk error of the receiver channel, because the parasitic capacitance of the measurement probe and PCB may affect the zero-crossing points.

The trans-impedance gain in the receiver channel was measured by applying an electrical pulse of $\sim 3ns$ FWHM to the input. In this measurement, the APD is biased by over $50V$, in which region the parasitic capacitance of the APD is minimal. The measured trans-impedance gain is $\sim 1.2M\Omega$ or $\sim 121dB\Omega$. The measured electrical noise of the channel was $\sim 80mV$RMS, or $\sim 70nA$RMS when referred to the input.

In the bandwidth measurements, the results of which are shown in Fig. 11, a white light source (representing a broadband noise spectrum) was applied to the APD in order to excite the receiver channel. The resulting output voltage spectrum is shown in this figure along with a trend line representing the frequency response of the channel. The measured bandwidth was $\sim 205MHz$ and the LC tank resonance frequency $\sim 155MHz$. According to simulation the bandwidth in the channel (without the effect of parasitic capacitances of the analog buffer output node and the measurement probe) is a little higher than this value and can be approximated to be $\sim 230-240MHz$.

B. Walk Error and DR Measurements

A MOS driver-based laser transmitter was used to study the walk error and DR of the proposed receiver channel. The laser ($LD905D1S$) can deliver pulses of different widths and rise times at a wavelength of around $905nm$. The maximum peak power it can deliver for the target pulse shapes is $\sim 20W$. Three laser pulse shapes were used to study the performance of the proposed receiver channel (Fig. 12), the DR and precision measurements being run for each pulse shape as explained below. These pulses were generated by changing the charging capacitor inside the laser driver loop. As explained in [47], the use of a smaller capacitance produces shorter pulses, but the peak power delivered is also reduced. The pulses were measured using a broadband optical probe ($25GHz$), while the bandwidth of the measurement oscilloscope was set to $250MHz$ (close to the bandwidth of the channel, solid lines). The dashed lines show the unfiltered version of the measured pulses.

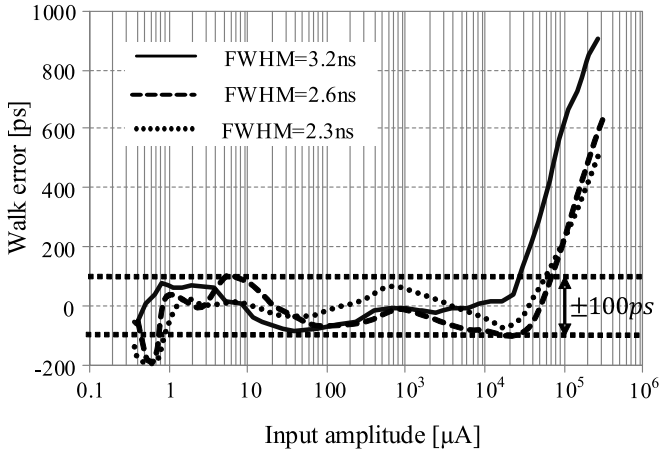

Fig. 13. Measured walk error using three different pulse shapes.

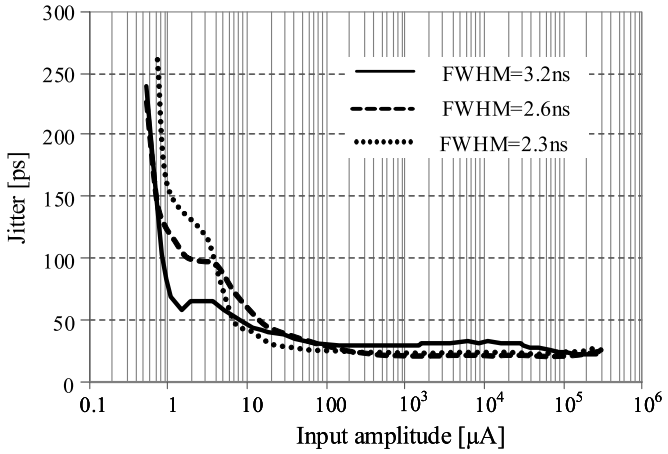

Fig. 14. The timing jitter (σ value) as a function of the input amplitude.

TABLE I
MEASURED DR IN WHICH THE WALK ERROR $< \pm 100ps$

Input Pulse width/Rise time	DR	Min. and max. detectable signals	Min SNR
3.2ns / 1.2ns	1:50,000	600nA : 30mA	9
2.6ns / 1.2ns	1:70,000	900nA : 64mA	13
2.3ns / 1.2ns	1:70,000	900nA : 64mA	13

The DR and walk error measurements were performed using the test environment shown in Fig. 9. An electrical start pulse sampled from the signal current of the laser is used to trigger the start channel of the TDC. The laser pulse amplitude was swept over a DR of $1:600,000$ using THORLABS neutral density filters and the APD bias voltage was set to $130V$ to ensure an internal gain of ~ 100 in the APD. Eight thousand measurements were run for each measurement point to achieve reliable statistical accuracy.

The results of the walk error measurements obtained using the pulse shapes described here are shown in Fig. 13 and summarized in Table I. The threshold level of the arming comparator was set to $SNR \geq\sim 8$(according to the simulations). As can be seen, the walk error remains within $\sim \pm 100ps$ in a DR of at least $1:50,000$ for all three input pulse types. These measurements show the effect of pulse variation on the performance of the receiver channel. The walk error curves approximately follow the same pattern especially in the case of $2.6ns$ and $2.3ns$, for which their rise times are equal. The minimum detectable signal is nevertheless increased as the input pulse becomes narrower because the $3.2ns$ pulse is a better match for the bandwidth of the receiver channel designed according to (7). In the $2.6ns$ and $2.3ns$ cases, the bandwidth of the channel cannot preserve the fast edge of the pulse completely and pulse detection/shaping is done while some portion of the pulse energy is being filtered. As can be seen in Fig. 13, however, the proposed technique can measure within a wider DR given a higher walk error tolerance.

C. Timing Jitter and Single-Shot Precision

The single-shot precision of the receiver was studied by measuring the timing jitter of the timing point, yielding the results shown in Fig. 14, in which eight thousand measurements were performed for each point and the standard deviations (σ value) of the measured stop times were calculated. According to Fig. 9, the other contributors to the measured timing jitter are jitter in the laser start pulse and jitter in the TDC itself. However, as long as the jitter from these two sources is sufficiently small relative to the timing jitter of the receiver channel, their impact will be negligible. The best measured timing jitter for all pulse shapes was $\sim 23ps$, obtained under conditions in which the jitter was limited due to the saturated rise time of the output pulse and limited precision of the measurement environment, as mentioned above.

The distribution of the measured stops is shown in Fig. 15 for four signal levels of the $3.2ns$ pulse shape. Improvement in the jitter can be seen, as the signal level increased relative to the noise. The shift seen in the peak point (around which the average point is located) represents the walk error.

D. Temperature Drift

The effect of temperature variation on the performance of the receiver channel was studied by placing the receiver PCB in an oven and sweeping the environment temperature from 0^oC to 50^oC in 10^oC steps. The rest of the system was kept outside the oven. The temperature drift of the APD gain was compensated for by $+0.45V/o_C$($130V$ at 23^oC) according to the datasheet. For each temperature point, a walk error measurement was run (same procedure as of Fig. 13). The results of these measurements, for which $2.6ns$ pulses were used, are shown in Fig. 16. The walk error of the receiver channel shows average temperature drift of $\sim 3.54ps/o_C$ for APD input currents below $100mA$ and $\sim 3.92ps/o_C$ for the whole range shown in the figure. As can be seen, the walk error exhibits a uniform behavior within the measured temperature range even when the signal level causes intense saturation of the channel.

TABLE II
SUMMARY OF THE MEASUREMENT RESULTS AND COMPARISON WITH THE STATE OF THE ART

	This work	[20]/2017	[29]/2018	[24]/2018	[23]/2009	[33]/2014	[1]/2013	[35]/2006
Technology	CMOS 0.35µm	CMOS 0.35µm	CMOS 0.18µm	CMOS 0.18µm[1]	CMOS 0.13µm	CMOS 0.35µm	CMOS 0.13µm[2]	BiCMOS 0.35 µm
Power Consumption (mW)	155	180	8*	29.8*	45	79	114	79
Bandwidth (MHz)	230	230	50	720	300	140	640	1600
Input Referred Noise Current (nA RMS)	70	100	10.8	170	95	17	119	190
Accuracy (mm) @ 23°c	±15	±4	NA	NA	±5.5	±210	NA	±5.5
DR	1:50,000	1:100,000	1:7,000	1:11,760	1:10,000	1:12,000	1:1600	1:1280
Precision (mm)	15(SNR=12)	26 (SNR=13)	NA	NA	38 (SNR=25)	NA	NA	33(SNR=10)
Min. detectable signal (µA)	0.6 (SNR=9)	1 (SNR=10)	0.4 (SNR=37)	NA	2 (SNR=20)	0.053 (SNR=3.3)	NA	1.9 (SNR=10)
Temperature Drift (mm)	±14.7	±18	NA	NA	±22.5	±45	NA	±7.7
Temperature Range (°C)	0 to +50	-20 to +50	NA	NA	-10 to +70	-40 to +85	NA	-30 to +60
Walk Compensation technique	Not needed	Pulse width and rise-time measurement	Front end Gain control	Front end Gain control	Rise-time measurement	Constant delay detection/ gain control	Font end Gain control	Not needed
Front end technique	Pulse-shaping	R-TIA	current mode TIA	Feedforward + R-TIA	R-TIA	C-TIA	R-TIA	Pulse-shaping

*front end only, [1]PIN input photodiode, [2]designed for a sampling-based receiver

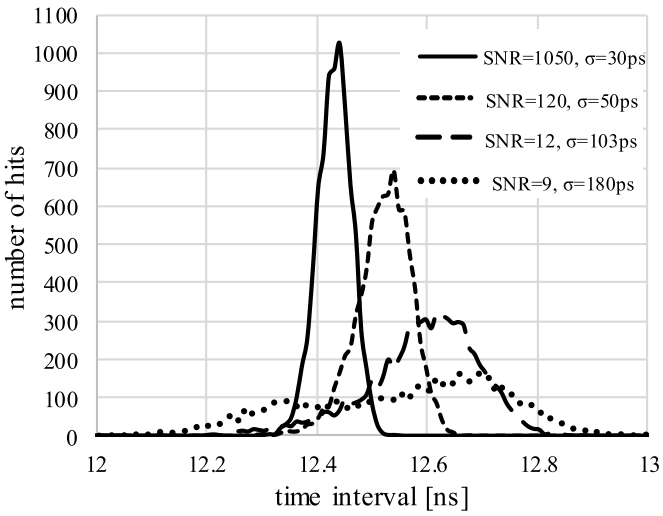

Fig. 15. The hit distribution of the measured stops for four different SNR.

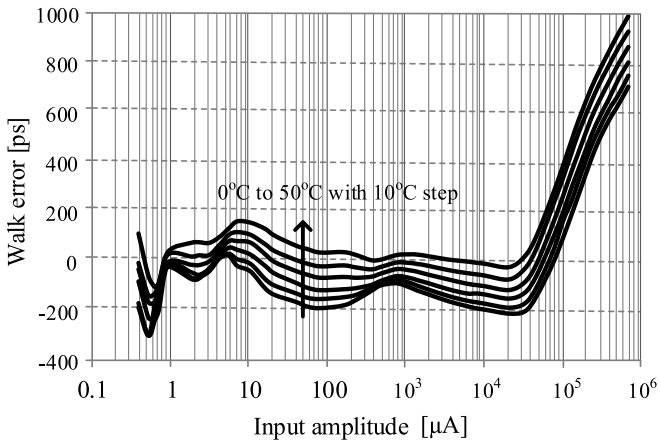

Fig. 16. Temperature drift of the timing walk error.

V. DISCUSSION

This paper has proposed a new type of receiver channel based on input pulse shaping and has reported on its design and measurements. The effect of input pulse variation and temperature drift on the performance of the receiver were also analyzed. Three pulse shapes with different widths and rise times were used in the measurements. Relatively consistent behavior was seen in terms of the walk error and timing jitter of the receiver channel for these three pulse shapes. In the case of $3.2ns$ pulses, a minimum detectable signal of $600nA$ ($SNR = 9$) was measured, while the DR, in which the walk error was less than $\pm 100ps$ ($\pm 15mm$), was $1 : 50,000$. The receiver channel showed a temperature drift of $\sim \pm 1.47cm$ in the temperature range 0°C – 50°C.

A summary of the measurement results by comparison with state-of-the-art receiver channels is shown in Table II. The key point here is that the proposed receiver channel does not employ any post-compensation or gain control techniques to achieve the present results. This important feature considerably reduces the total complexity of the TOF system and the total measurement time. Furthermore, the receiver channel can be integrated into a simplified TDC on a single die, since the only parameter to be discriminated is the zero-crossing point of the converted pulse.

The receiver proposed in [33], for example, incorporated a C-TIA for the front end to achieve a very low noise level and used a constant delay detection method to compensate for the walk error, which needs collaboration with the TDC unit. Another design, reported in [29], adopted front end gain control and achieved a DR of 1:7,000, which is relatively wide for gain control-based front ends. The measurement process nevertheless needs extra information from the signal to set the proper gain for each measurement point.

The receiver reported in [35] is comparable to that proposed work here since it is the only one to use front-end pulse shaping immediately at the input. The minimum detectable signal in that design is limited to $\sim 2\mu A$ due to the use of a relatively small front-end resistor ($1.2k\Omega$) which generates a relatively high level of noise at the input. Another issue in that design is that the current-to-voltage conversion takes place immediately at the input to the receiver channel, which limits the maximum acceptable input current that can be detected. Both of these problems were addressed here by combining the LC resonator with a non-linear feedback TIA.

APPENDIX

According to Fig. 3, and assuming that the input current is sourced to the input node, the current flowing to the feedback resistor (R_F) can be designated as

$$I_{RF} = I_{in,TIA} - I_{PF}, \tag{14}$$

We assume that the input current is large enough to turn on the transistor M_{PF}. Then we have:

$$\begin{cases} V_{SG,PF} = R_F I_{RF} \\ I_{PF} = \frac{K_P}{2}\left(V_{SG,PF} - |V_{TH,P}|\right)^2 R_F I_{in,TIA} \geq |V_{TH,P}| \end{cases}, \tag{15}$$

where I_{PF} and $V_{SG,PF}$ are the drain current and source-gate voltage of the M_{PF} transistor respectively. By substituting (15) in (14) and re-arranging it, the result will be

$$\frac{K_P}{2}R_F^2 I_{RF}^2 + \left(1 - K_P|V_{TH,P}|R_F\right) I_{RF} + \frac{K_P}{2}V_{TH,P}^2 - I_{in,TIA} = 0, \tag{16}$$

Equation (16) is a quadratic equation with respect to I_{RF}, and solving it for I_{RF} will result in

$$I_{RF} = \frac{K_P|V_{TH,P}|R_F - 1 + \sqrt{1 + 2K_P R_F(R_F I_{in,TIA} - |V_{TH,P}|)}}{K_P R_F^2}, \tag{17}$$

which denotes a square root relation between I_{RF} and I_{in}. A similar equation can be derived when the transistor M_{NF} is turned on for the sinking input currents from the input node (given that the TIA input current is a bipolar signal). The square root function of I_{RF} when the input current is large enough can be seen clearly in Fig. 4.

REFERENCES

[1] T.-H. Ngo, C.-H. Kim, Y. J. Kwon, J. S. Ko, D.-B. Kim, and H.-H. Park, "Wideband receiver for a three-dimensional ranging LADAR system," *IEEE Trans. Circuits Syst. I, Reg. Papers*, vol. 60, no. 2, pp. 448–456, Feb. 2013.

[2] S. Donati, *Electro-Optical Instrumentation: Sensing and Measuring With Lasers*. London, U.K.: Pearson, 2004.

[3] T. Bosch, "Laser ranging: A critical review of usual techniques for distance measurement," *Opt. Eng.*, vol. 40, no. 1, p. 10, Jan. 2001.

[4] T. Ruotsalainen, P. Palojarvi, and J. Kostamovaara, "A wide dynamic range receiver channel for a pulsed time-of-flight laser radar," *IEEE J. Solid-State Circuits*, vol. 36, no. 8, pp. 1228–1238, Aug. 2001.

[5] V. C. Coffey, "Imaging in 3-D: Killer apps coming soon to a device near you!," *Opt. Photon. News*, vol. 25, no. 6, p. 36–46, Jun. 2014.

[6] B. Schwarz, "LIDAR: Mapping the world in 3D," *Nature Photon.*, vol. 4, no. 7, pp. 429–430, 2010.

[7] Y. Tang *et al.*, "Vision-aided multi-UAV autonomous flocking in GPS-denied environment," *IEEE Trans. Ind. Electron.*, vol. 66, no. 1, pp. 616–626, Jan. 2019.

[8] C. Mallet and F. Bretar, "Full-waveform topographic lidar: State-of-the-art," *ISPRS J. Photogramm. Remote Sens.*, vol. 64, no. 1, pp. 1–16, Jan. 2009.

[9] A. Ullrich, "Resolving range ambiguities in high-repetition rate airborne light detection and ranging applications," *J. Appl. Remote Sens.*, vol. 6, no. 1, Jul. 2012, Art. no. 063552.

[10] K. Thiel and A. Wehr, "Performance capabilities of laser scanners—An overview and measurement principle analysis," *Int. Arch. Photogramm., Remote Sens. Spatial Inf. Sci.*, vol. 36, no. 8, pp. 14–18, 2004.

[11] J. M. Rüeger, *Electronic Distance Measurement: An Introduction*. Berlin, Germany: Springer-Verlag, 1996.

[12] P. Palojarvi, K. Maatta, and J. Kostamovaara, "Pulsed time-of-flight laser radar module with millimeter-level accuracy using full custom receiver and TDC ASICs," *IEEE Trans. Instrum. Meas.*, vol. 51, no. 5, pp. 1102–1108, Oct. 2002.

[13] K. Asaka, T. Yanagisawa, and Y. Hirano, "1.5-μm eye-safe coherent lidar system for wind velocity measurement," in *Proc. Lidar Remote Sens. Ind. Environ. Monitor.*, Feb. 2001, pp. 321–328.

[14] G. M. Williams and A. S. Huntington, "Probabilistic analysis of linear mode vs. Geiger mode APD FPAs for advanced LADAR enabled interceptors," *Proc. SPIE Spaceborne Sensors III*, vol. 6220, May 2006, Art. no. 622008.

[15] G. Limi Jaya, S. Chen, and L. Siek, "The design of clocked-comparator-based time-interval measurement circuit for pulse ToF measurement," *IEEE Sensors J.*, vol. 17, no. 20, pp. 6699–6706, Oct. 2017.

[16] H. N. Burns, "System design of a pulsed laser rangefinder," *Opt. Eng.*, vol. 30, no. 3, pp. 323–330, 1991.

[17] M. L. Simpson, C. L. Britton, A. L. Wintenberg, and G. R. Young, "An integrated, CMOS, constant-fraction timing discriminator for multichannel detector systems," *IEEE Trans. Nucl. Sci.*, vol. 42, no. 4, pp. 762–766, Aug. 1995.

[18] M. Hintikka and J. Kostamovaara, "Experimental investigation into laser ranging with sub-ns laser pulses," *IEEE Sensors J.*, vol. 18, no. 3, pp. 1047–1053, Feb. 2018.

[19] P. Palojarvi, T. Ruotsalainen, and J. Kostamovaara, "A 250-MHz BiCMOS receiver channel with leading edge timing discriminator for a pulsed time-of-flight laser rangefinder," *IEEE J. Solid-State Circuits*, vol. 40, no. 6, pp. 1341–1349, Jun. 2005.

[20] S. Kurtti, J. Nissinen, and J. Kostamovaara, "A wide dynamic range CMOS laser radar receiver with a time-domain walk error compensation scheme," *IEEE Trans. Circuits Syst. I, Reg. Papers*, vol. 64, no. 3, pp. 550–561, Mar. 2017.

[21] S. Kurtti, J.-P. Jansson, and J. Kostamovaara, "A CMOS receiver—TDC chip set for accurate pulsed TOF laser ranging," *IEEE Trans. Instrum. Meas.*, early access, May 22, 2019, doi: 10.1109/TIM.2019.2918372.

[22] S. Kurtti and J. Kostamovaara, "An integrated laser radar receiver channel utilizing a time-domain walk error compensation scheme," *IEEE Trans. Instrum. Meas.*, vol. 60, no. 1, pp. 146–157, Jan. 2011.

[23] J. Nissinen, I. Nissinen, and J. Kostamovaara, "Integrated receiver including both receiver channel and TDC for a pulsed time-of-flight laser rangefinder with cm-level accuracy," *IEEE J. Solid-State Circuits*, vol. 44, no. 5, pp. 1486–1497, May 2009.

[24] C. Hong, S.-H. Kim, J.-H. Kim, and S. M. Park, "A linear-mode LiDAR sensor using a multi-channel CMOS transimpedance amplifier array," *IEEE Sensors J.*, vol. 18, no. 17, pp. 7032–7040, Sep. 2018.

[25] H. Zheng, R. Ma, M. Liu, and Z. Zhu, "A linear dynamic range receiver with timing discrimination for pulsed TOF imaging LADAR application," *IEEE Trans. Instrum. Meas.*, vol. 67, no. 11, pp. 2684–2691, Nov. 2018.
[26] H. Zheng, R. Ma, M. Liu, and Z. Zhu, "A linear-array receiver analog front-end circuit for rotating scanner LiDAR application," *IEEE Sensors J.*, vol. 19, no. 13, pp. 5053–5061, Jul. 2019.
[27] T. Ruotsalainen, P. Palojarvi, and J. Kostamovaara, "A current-mode gain-control scheme with constant bandwidth and propagation delay for a transimpedance preamplifier," *IEEE J. Solid-State Circuits*, vol. 34, no. 2, pp. 253–258, Feb. 1999.
[28] S. Kurtti and J. Kostamovaara, "Laser radar receiver channel with timing detector based on front end unipolar-to-bipolar pulse shaping," *IEEE J. Solid-State Circuits*, vol. 44, no. 3, pp. 835–847, Mar. 2009.
[29] R. Ma, M. Liu, H. Zheng, and Z. Zhu, "A 77-dB dynamic range low-power variable-gain transhipped amplifier for linear LADAR," *IEEE Trans. Circuits Syst. II, Exp. Briefs*, vol. 65, no. 2, pp. 171–175, Mar. 2018.
[30] R. Ma, M. Liu, H. Zheng, and Z. Zhu, "A 66-dB linear dynamic range, 100-dBΩ transimpedance gain TIA with high-speed PDSH for LiDAR," *IEEE Trans. Instrum. Meas.*, vol. 69, no. 4, pp. 1020–1028, Apr. 2020.
[31] H. Zheng, R. Ma, M. Liu, and Z. Zhu, "High sensitivity and wide dynamic range analog front-end circuits for pulsed TOF 4-D imaging LADAR receiver," *IEEE Sensors J.*, vol. 18, no. 8, pp. 3114–3124, Apr. 2018.
[32] A. Trabelsi and M. Boukadoum, "Comparison of two CMOS front-end transimpedance amplifiers for optical biosensors," *IEEE Sensors J.*, vol. 13, no. 2, pp. 657–663, Feb. 2013.
[33] H.-S. Cho, C.-H. Kim, and S.-G. Lee, "A high-sensitivity and low-walk error LADAR receiver for military application," *IEEE Trans. Circuits Syst. I, Reg. Papers*, vol. 61, no. 10, pp. 3007–3015, Oct. 2014.
[34] R. J. van de Plassche and P. Baltus, "An 8-bit 100-MHz full-Nyquist analog-to-digital converter," *IEEE J. Solid-State Circuits*, vol. 23, no. 6, pp. 1334–1344, Dec. 1988.
[35] J. Pehkonen, P. Palojarvi, and J. Kostamovaara, "Receiver channel with resonance-based timing detection for a laser range finder," *IEEE Trans. Circuits Syst. I, Reg. Papers*, vol. 53, no. 3, pp. 569–577, Mar. 2006.
[36] B. Razavi, *Design of Integrated Circuits for Optical Communications*. Hoboken, NJ, USA: Wiley, 2012.
[37] E. Säckinger, *Broadband Circuits for Optical Fiber Communication*. Hoboken, NJ, USA: Wiley, 2005.
[38] R. Ziemer and W. H. Tranter, *Principles of Communications: System Modulation and Noise*. Hoboken, NJ, USA: Wiley, 2006.
[39] A. Baharmast and J. Kostamovaara, "A low noise front end transimpedance amplifier channel for a pulsed time-of-flight laser radar," in *Proc. 13th Conf. Res. Microelectron. Electron. (PRIME)*, Jun. 2017, pp. 285–288.
[40] A. Baharmast, T. Ruotsalainen, and J. Kostamovaara, "A low noise, wide dynamic range TOF laser radar receiver based on pulse shaping techniques," in *Proc. IEEE Int. Symp. Circuits Syst. (ISCAS)*, 2018, pp. 1–5.
[41] A. Baharmast and J. Kostamovaara, "Noise considerations in pulse-shaping based TIA channel designed for a pulsed TOF laser radar receiver," in *Proc. IEEE Nordic Circuits Syst. Conf. (NORCAS)*, Oct. 2018, pp. 1–6.
[42] A. A. Abidi, "On the choice of optimum FET size in wide-band transimpedance amplifiers," *J. Lightw. Technol.*, vol. 6, no. 1, pp. 64–66, Jan. 1988.
[43] S. Galal and B. Razavi, "10-Gb/s limiting amplifier and laser/modulator driver in 0.18-μm CMOS technology," *IEEE J. Solid-State Circuits*, vol. 38, no. 12, pp. 2138–2146, Dec. 2003.
[44] J. Doernberg, P. R. Gray, and D. A. Hodges, "A 10-bit 5-Msample/s CMOS two-step flash ADC," *IEEE J. Solid-State Circuits*, vol. 24, no. 2, pp. 241–249, Apr. 1989.
[45] P. E. Allen and D. R. Holberg, *CMOS Analog Circuit Design*. Amsterdam, The Netherlands: Elsevier, 2011.
[46] J.-P. Jansson, A. Mantyniemi, and J. Kostamovaara, "A CMOS time-to-digital converter with better than 10 ps single-shot precision," *IEEE J. Solid-State Circuits*, vol. 41, no. 6, pp. 1286–1296, Jun. 2006.
[47] J. Nissinen and J. Kostamovaara, "A high repetition rate CMOS driver for high-energy sub-ns laser pulse generation in SPAD-based time-of-flight range finding," *IEEE Sensors J.*, vol. 16, no. 6, pp. 1628–1633, Mar. 2016.

Aram Baharmast (Student Member, IEEE) received the M.Sc. degree in electronics from the Iran University of Science and Technology (IUST), Tehran, Iran, in 2013. He is currently pursuing the Dr.Tech. degree in electronics with the University of Oulu. He has been with the Circuits and Systems Research Unit (CAS), University of Oulu, since 2016. His main research interests include analog, digital, and mixed-signal integrated circuits especially for pulsed time-of-flight (TOF) techniques.

Sami Kurtti was born in Kuusamo, Finland, in 1979. He received the M.Sc.Eng. and Dr.Tech degrees in electrical engineering from the University of Oulu, Finland, in 2004 and 2013, respectively. He was a Research Scientist from 2004 to 2013 and has been a Post-Doctoral Researcher with the Circuits and Systems Research Unit, University of Oulu, since 2013. His interests include the development of analogue and mixed-signal integrated circuits and structures for pulsed time-of-flight laser rangefinders.

Juha Kostamovaara (Senior Member, IEEE) received the Dr.Eng. degree in electrical engineering from the University of Oulu, Oulu, Finland, in 1987. He has hold the Academy Professorship position nominated by the Academy of Finland from 2006 to 2011 and then for the second time from 2012 to 2017. He currently holds a Professorship in electronics with the Circuits and Systems Research Unit, University of Oulu. His main research interest is in the development of pulsed time-of-flight devices, circuits, and systems for electronic and optoelectronic measurements.